

Infrared Detector Assemblies for the Tropospheric Emission Spectrometer

Carl F. Bruce - 818.354.5480 email: Carl.F.Bruce-Jr@jpl.nasa.gov
Jet Propulsion Laboratory, Pasadena, CA 91109

J. Bajaj, D. Lee, T.A. Pepper, G. Chu, W.V. McLevige, D.D. Edwall, L.A. McGregor, W. Weissbard, G. Hildebrandt,
J.D. Blackwell, S. Bhargava, V. Gil, D.E. Cooper, K. Spariosu, J. M. Arias, W.E. Tennant and K. Vural
Rockwell Science Center, LLC, Thousand Oaks, CA 91360

L. Shin
Boeing Electronic Systems & Missile Defense, Anaheim, CA 92803

Abstract—This paper provides an overview of the Tropospheric Emission Spectrometer (TES) and its mission, as a part of NASA's Earth Observing System (EOS). It will present, in detail, the design, fabrication and performance of the Infrared Focal Plane Assembly (IRFPA) used in this instrument. There are four IRFPAs, each covering one of four infrared spectral bands (3.3-5.3, 5.1-9.1, 8.3-12.2 and 11.1-15.4 μm). Each IRFPA consists of a 16-element detector array, a detector package, and a differential J-FET buffered transimpedance amplifier for each element with a flex-print cable that connects the cold detector package to the warm amplifier board.

INTRODUCTION

TES is an infrared (3.3-15.4 micron), high resolution (0.25 cm^{-1}), imaging Fourier Transform Spectrometer (FTS). TES is intended to measure essentially all infrared-active molecules present in the Earth's Troposphere.¹ The primary function of TES is to map the global, three-dimensional distribution, of concentration of a large number of molecules important to tropospheric physics and chemistry. These important molecular species include: ozone, nitric oxide, nitrogen dioxide, nitric acid, water vapor, carbon monoxide, methane and carbon dioxide for the determination of atmospheric temperature. TES will accomplish this through a series of nadir and limb measurements using 16 pixel, linear detector arrays in each of four infrared bands. In the limb view the 16 pixels will rise from the earth's surface to ~30 km at the top of the troposphere. Each pixel will have a spatial extent of 2.3 km high by 23 km parallel to the earth's surface at the limb. In the nadir view the pixel IFOV is 0.5 km by 5.0 km.

Each of the 64 pixels has its own preamplifier and signal chain feeding 64 parallel 16-bit A/D converters. A differential J-FET pair individually buffers each of the 16 elements in the four arrays. Large value resistors ~1E6 to ~1E8 Ohms provide the signal feedback to the detectors in a

transimpedance amplifier configuration. The above components are mounted to a ceramic multilayer board (CMLB) and housed in a Be package which will be cooled to 65K. The remainders of the preamplifier circuits are housed near by in a 240K, Al chassis. These amplified signals are then passed to a near room temperature electronic assembly for the remaining signal filtering, gain and digitization. The maximum preamplifier gain is set to ensure that the system will not saturate under maximum signal conditions. The equivalent electrical bandwidth of each optical band is determined by the scan velocity of the spectrometer's retro-reflectors and the alias order. The shortest wavelength band has the highest electrical frequency requirements, which drive the requirements for preamplifier and detector architecture. The longest waveband pushes PV HgCdTe detector sensitivity requirements to near theoretical levels.

The following section details the TES mission and instrument architecture. Section 2.0 details the IRFPA performance requirements. Section 3.0 provides an overview of the detector architecture and fabrication. Section 4.0 covers the detector design. Section 5.0 details the detector array performance for all four bands. Section 6.0 presents the preamplifier design and section 7.0 details the results of IRFPA level radiation tests. Section 8.0 presents a summary of this work with suggested future directions for this technology.

1.0 THE TES MISSION and INSTRUMENT ARCHITECTURE

The TES instrument is one of four instruments scheduled to fly aboard the EOS, CHEM satellite. CHEM is currently scheduled for launch in January of '02. The goals of the EOS program have been summarized in five "research questions" as reviewed in the TES Science Requirements.

What are the nature and extent of land-cover and land-use change and the consequences for sustained productivity?

- 1) How can we enable regionally useful forecasts of precipitation and temperature on seasonal to inter-annual time frames?
- 2) Can we learn to predict natural hazards and mitigate natural disasters?
- 3) What are the causes and impacts of long-term climate variability and can we distinguish natural from human induced-drivers?
- 4) How and why are concentrations and distributions of atmospheric ozone changing?

Although TES may contribute to answering all five questions, TES is specifically designed to address item five and it will do this by providing global maps of chemical concentration through out the troposphere every five days. In order to accomplish this feat, TES has been designed as a high resolution FTS which is capable of collecting infrared spectra over a large region of the spectrum from 3.3 to 15.4 microns. The TES instrument is shown in schematic form in Figure 1.0.

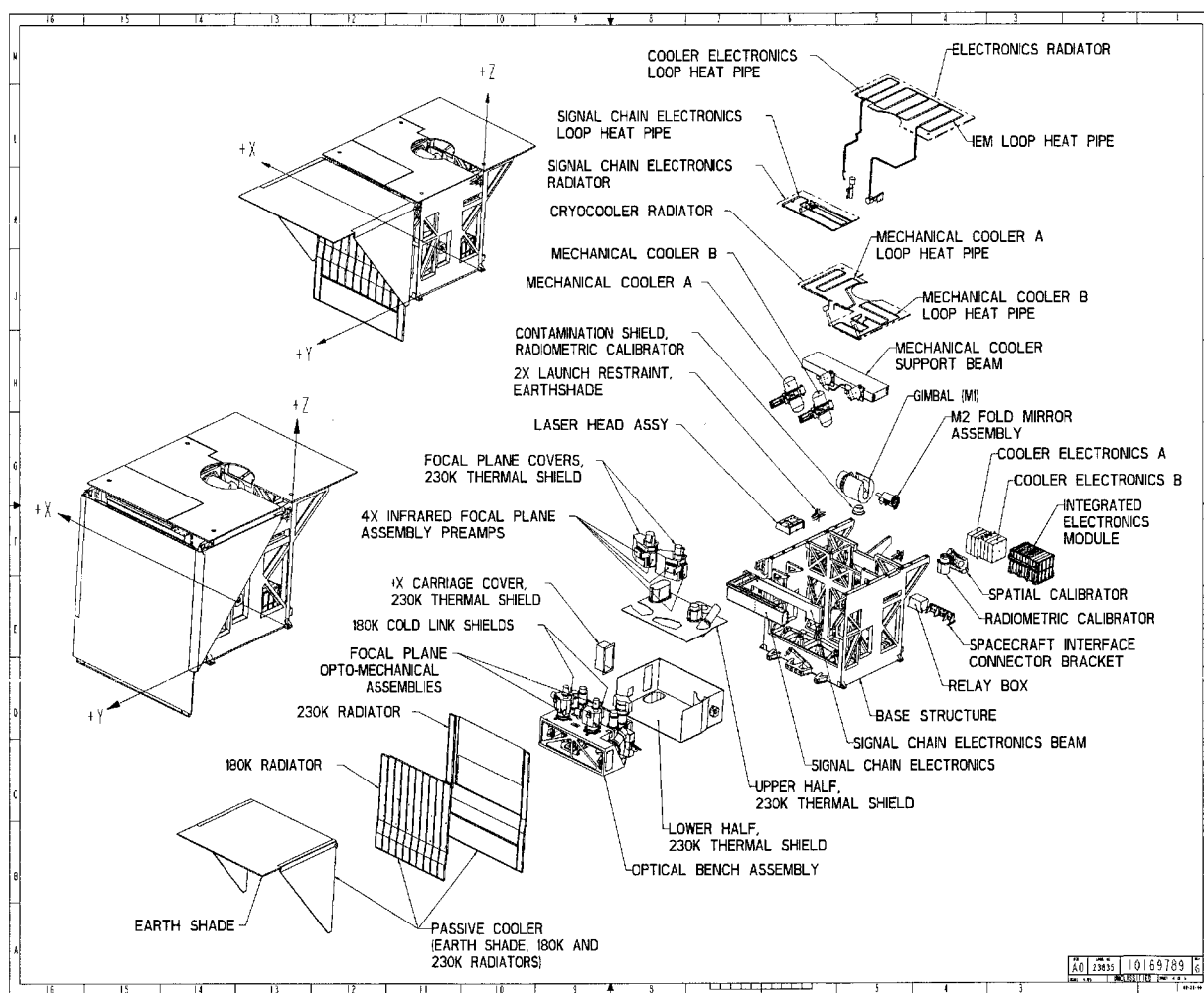


Figure 1.0 - TES Instrument Schematic

Primary subsystems of TES include:

The thermal control system which encompasses every aspect of the instrument design as well as two TRW cryocoolers which will maintain the infrared detectors and reimaging optics at 65K. In addition, two large radiators provide cooling for the interferometer to 180K and for rejection of heat from the instrument electronics.

The pointing control system, which allows TES to track its image point during the nadir acquisition, obtain limb pointing, view calibration targets as well as acquire targets of opportunity across-track.

The calibration system, which will provide reference signals for the radiometric calibration every 90 seconds within the global survey. The system will also provide the capability for a multi-point linearity calibration and in-flight mapping of the instrument field of view response.

The integrated electronics system, based upon a VME buss architecture, includes most all of the instrument electronics, the power subsystem and its elements as well as the control system for the interferometer translator. The interferometer and optical layout of TES is presented in simplified form in Figure 2.0

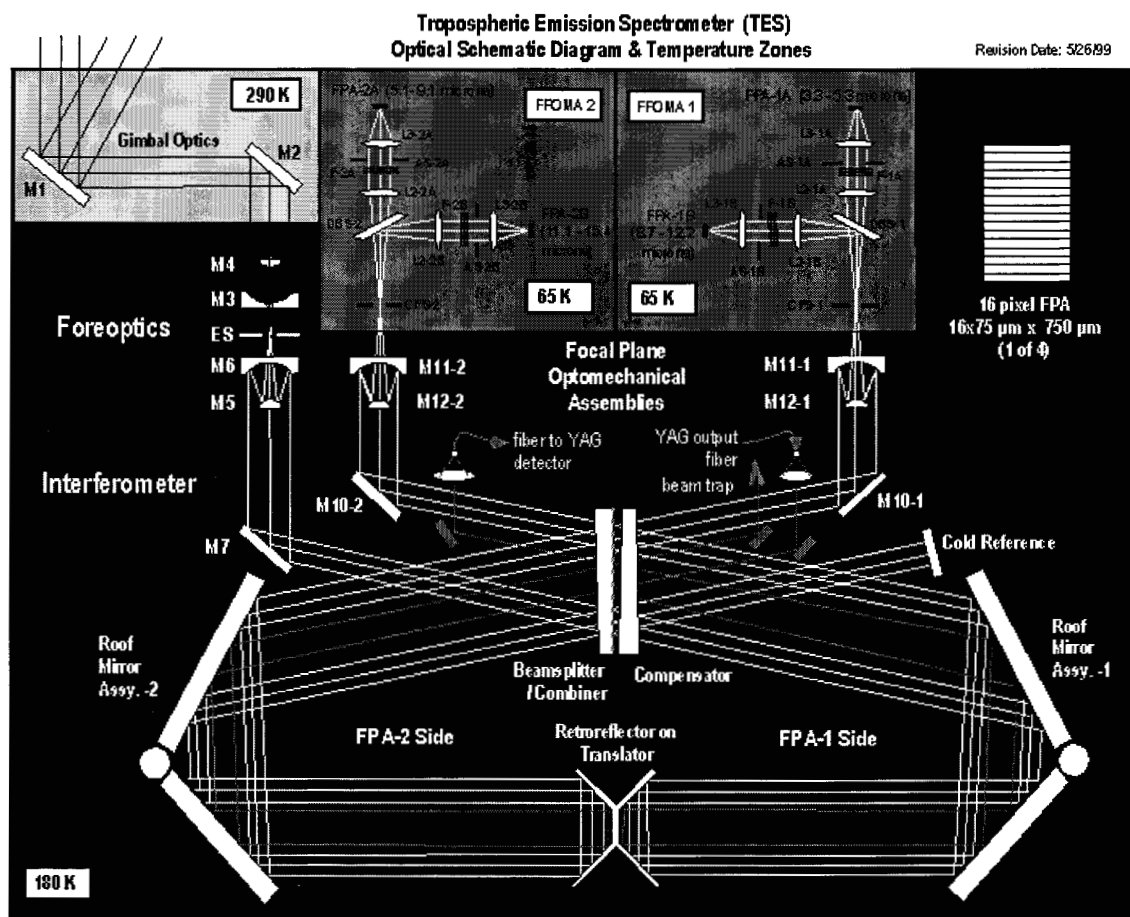
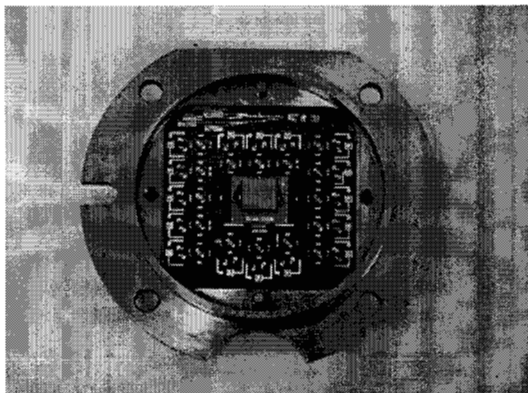


Figure 2.0 - TES Optical Layout and Temperature Zones

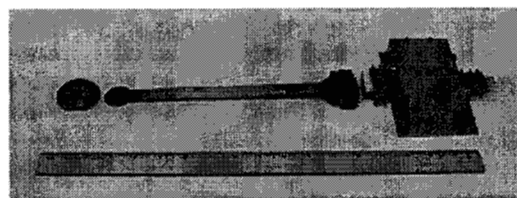
The Focal Plane Opto-Mechanical Assemblies (FPOMA) constructed at the Space Dynamics Laboratory house the infrared detector assemblies, which are provided under contract with Rockwell International, Science Center and its subcontractors.

These IRFPAs are implemented with a detector amplifier topology that includes one differential J-FET buffered transimpedance amplifier (TIA) per detector element. The J-FETS, the feedback resistor, and any decoupling capacitors are placed with the linear detector arrays onto a ceramic, multilayer board (CMLB). A Be flange is mated with the CMLB by an adhesive joint. The Be provides the

mechanical and thermal interfaces for the detector package. This detector package is shown in Picture 1.0. A low thermal conductance, flexprint cable, made of Constantan and Kapton, will connect the detector package with the amplifier board. The amplifier-board contains the 16 Harris, HA5104 operational amplifiers and J-FET buffer loads. The amplifier board will also develop a low noise supply voltage for the cryogenic J-FET (U401). This IRFPA is shown in Picture 2.0.



Picture 1.0 – Detector Package



Picture 2.0 – IRFPA

2.0 DETECTOR PERFORMANCE REQUIREMENTS

The performance requirements for the TES infrared detector assemblies represent the completion of a series of design trades that begin with the TES, instrument level, and science requirements. These requirements define the etude of the system, its' optical and electrical passbands, its' end-to-end linearity and numerous other instrument parameters. Some of the detector requirements for the TES program are summarized in Table 1.0.

Table 1.0
TES, Detector Requirements

Parameter	IRFPA 1A	IRFPA 2A	IRFPA 1B	IRFPA 2B
Temperature (K)	65	65	65	65
Detector Optical Area (μm^2)	75 x 750	75 x 750	75 x 750	75 x 750
Detector Band Pass (μm)	3.3 - 5.3	5.1 - 9.1	8.3 - 12.2	11.1 - 15.5
Peak $D^*(\text{Hz}^{-1/2} \text{ cm}^2/\text{W})$ (goal)	1.0E13	3.9E12	1.5 E12	3.9 E11
Max Background Flux (ph/cm ² /s)	1.5E15	9.4E15	1.7E16	2.5E16
Min Background Flux (ph/cm ² /s)	6.5E10	9.5E12	1.0E14	1.0E14
External QE (%)	70	65	65	60
$R_0 A_{\text{opt}} (\text{Ohm-cm}^2)$	1.0E8	5.0E3	300.0 (goal)	10.0 (goal)

The detector operating temperature requirement represents a complex trade between cryocooler technology, instrument power, J-FET noise, detector capacitance and detector noise. Modeling indicates that lower detector temperature improves detector performance for bands 1B, 2A and 2B but result in higher J-FET noise, which, ultimately limits the sensitivity of the 1A band detector and its' preamplifier. The calculated detectivity is plotted as a function of detector package temperature for each of the four bands in Figure 3.0.

The final F-number of the reimaging optics and the detector area are chosen to maintain the required etuandue of the

system. In order to minimize of detector capacitance as well improve producibility, a smaller detector area is preferred. In order to increase tolerances for detector alignment a larger F-number is preferred. The compromise of these two factors resulted in a system at F-number =2.0 with alignment requirements at the detector on the order of +/-5 microns. This F-number places the required detector area at 75 x 750 microns.

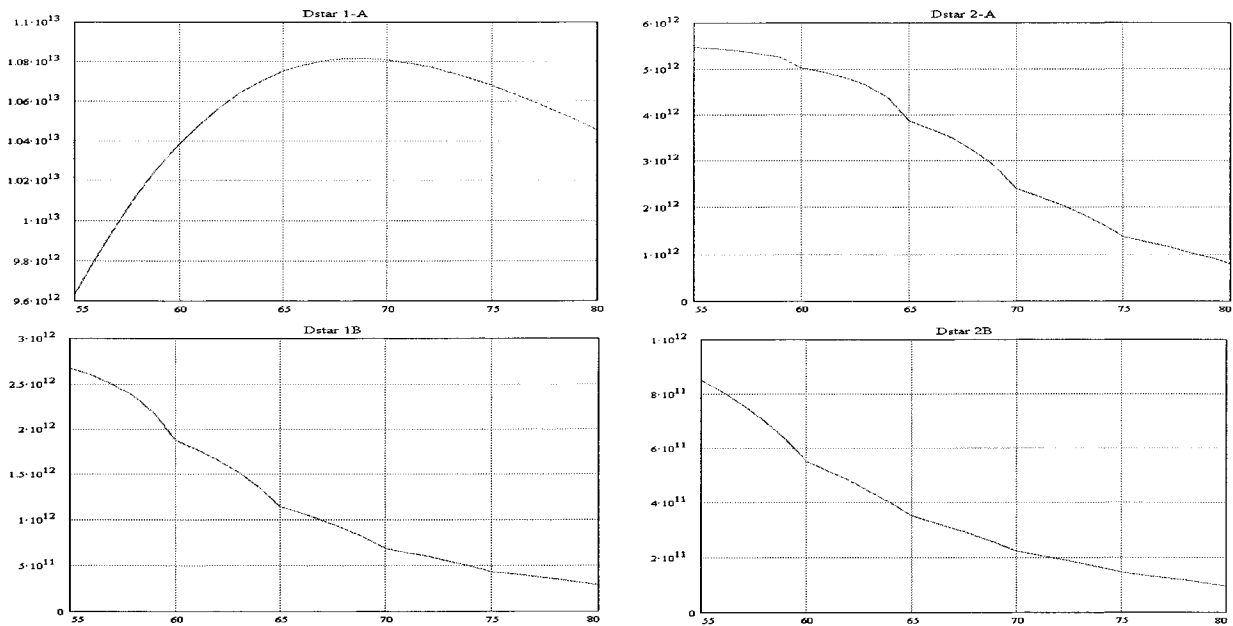


Figure 3.0 – Calculated detectivity for each IRFPA as a function of temperature.

The TES science requirements state that the instrument shall not saturate under maximum signal conditions and that a S/N greater than 30 is required of all observations. The resulting detectivity of each IRFPA is determined by the amplifier topology and two resultant design principles. First, choose the largest preamplifier gain possible without saturating the signals for the maximum flux case. The maximum flux case occurs when the instrument, at nominal temperature, is viewing the 340 Kelvin calibration source while at the interferometer zero path difference. Second, maximize detector responsivity and detector dynamic resistance so that detector sensitivity is as high as possible.

In order to realize these goals a novel design approach was implemented to improve the producibility of large area HgCdTe detector and to minimize detector capacitance so that detector thermal noise would limit sensitivity under the zero flux condition. Rockwell Science Center was chosen by competitive bid to implement these detectors. A description of their baseline detector architecture and fabrication follows.

3.0 DETECTOR ARCHITECTURE and FABRICATION

The detector arrays for TES are based on HgCdTe (MCT) double-layer planar heterostructure (DLPH) architecture. A cross sectional schematic of the device is illustrated in Fig. 4.0. An important feature of the DLPH approach is the planar P/N device geometry with a wide-bandgap surface layer covering the narrow-bandgap active layer. The layers are all grown n-type *in situ* by molecular beam epitaxy

(MBE), ensuring that the critical heterointerface is never exposed to ambient contamination. This mitigates many of the surface issues, which plagued HgCdTe PV detectors in the past.

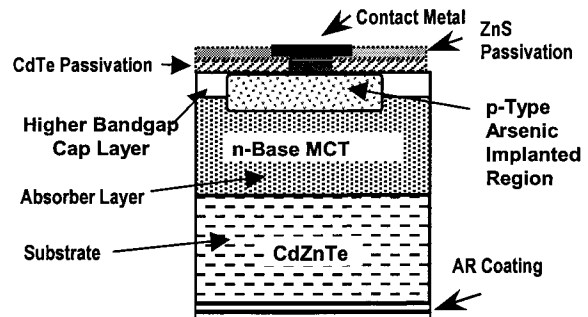


Figure 4.0 – DLPH Cross Section

The formation of planar p-on-n photodiodes is achieved by selective area, arsenic (As) ion-implantation through the cap layer into the narrow gap base layer. The implantation step is followed by a two-step thermal anneal under Hg overpressure. A high temperature anneal in Hg vapor activates the dopant by substituting arsenic atoms on the Te sublattice. During the high temperature portion of the anneal, some cadmium and mercury interdiffusion occurs between the absorber and cap layers. However, Rockwell has reported that no significant movement is observed in the arsenic profile². A lower temperature anneal, performed immediately after the high temperature anneal, limits the Hg vacancies formed in the HgCdTe lattice during growth and high temperature annealing step. A thin polycrystalline MBE deposited CdTe layer provides the device passivation. Holes

are then etched in the CdTe layer, and ohmic contacts are deposited. The wafer is then over-coated with ZnS, which serves to provide better adhesion for the interconnect metal. After etching via holes in the ZnS to expose the ohmic contact metal, the interconnect-metal is deposited. The process is completed with a backside polish, dicing into separate arrays and Process Evaluation Chips (PECs), and deposition of a backside anti-reflection (AR) coating.

4.0 DETECTOR DESIGN

For this process the presence of localized defects results in area-dependent detector performance, with small area detectors ($<1\text{E-}5\text{ cm}^2$) having considerably better performance than larger area detectors.³ Reducing the electrical P/N junction area of the diode reduces the probability that a given defect will coincide with the junction, thereby minimizing the effects caused by localized

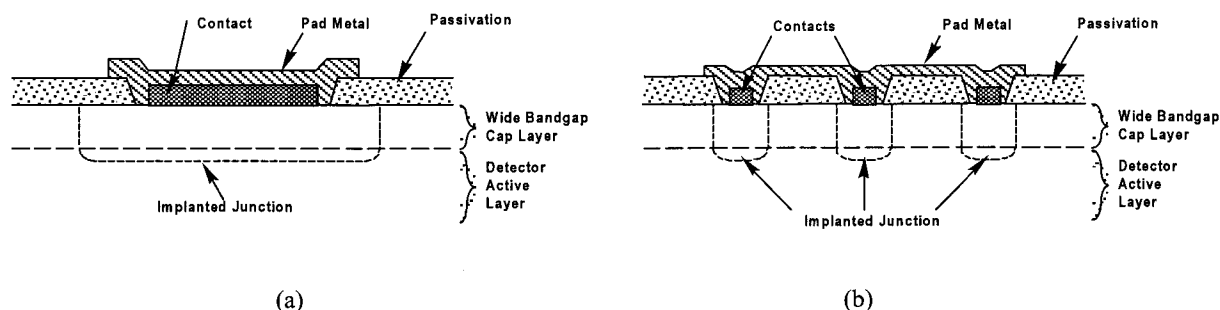


Figure 5.0 - Cross section and top view for DLPH conventional (a) and lateral collection (b) diode architectures.

defects. By taking advantage of lateral current collection, which takes place within a few diffusion lengths of a junction, large optically sensitive areas can be achieved with small junctions. Cross sections comparing conventional and lateral collection diodes are shown in Figure 5.0.

The effects of lateral collection on detector spatial response may be *illustrated* using a simplified 1-D model. Figure 6.0 (a) shows the spatial response of a 75-micron pixel with varying diffusion lengths. As the diffusion length becomes small as compared to the junction length the junction length limits the pixel spatial response which becomes more rectangular. Figure 6.0 (b) shows the spatial response of a pixel with a constant diffusion length but where the pixel junction length varies. As the junction length becomes smaller than the diffusion length the diffusion length limits the pixel response⁴. Thus for infinitesimal junctions the pixel can still have significant spatial response.

In an effort to validate this technology approach, JPL contracted with the Rockwell Science Center to produce VLWIR process evaluation chips (PECs) with variable area and large area (50 X 500 microns) arrays. The results of that study confirmed the improvements in device performance and yield⁵. During this study effort a sample PEC was tested at JPL. Figure 7.0 show IV plots over temperature for a 128-micron lateral area collection (LC-128) device and a 125-micron device with the conventional junction design. The improvements in the dark current characteristics are very notable as well as the higher

breakdown voltage for this lateral collection device. Effects of series resistance are apparent in the forward bias condition.

With proper design the optical collection area of a detector can be substantially larger than its electrical junction area. While the P/N junction in the conventional diode is formed by a contiguous implant, the lateral collection diode is split into a number of small area implants separated by a distance on the order of one minority carrier diffusion length. By configuring an array of very small diodes interconnected in parallel by metallization, a large-optical-area photodetector can be fabricated with the small electrical junction area. The advantages of reduced dark current, high resistance, and lower capacitance may be realized. The difference between the optical and electrical junction areas can easily be an order of magnitude. An advantage of the DLPH architecture is its direct compatibility with implementing lateral collection concepts, since the structure is planar and the P/N junction regions are formed by implantation and annealing.

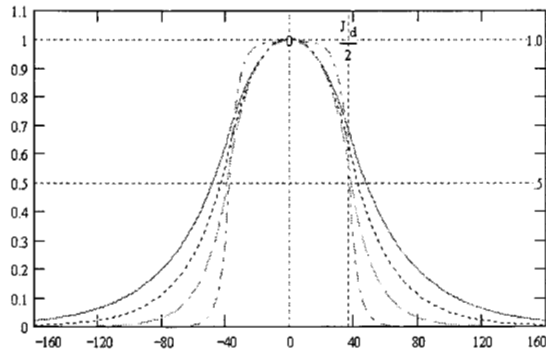
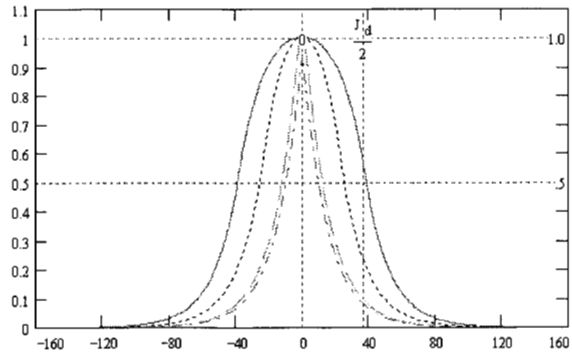


Figure 6.0. - (a) Spatial response as diffusion length varies.



(b) Spatial response as junction length varies.

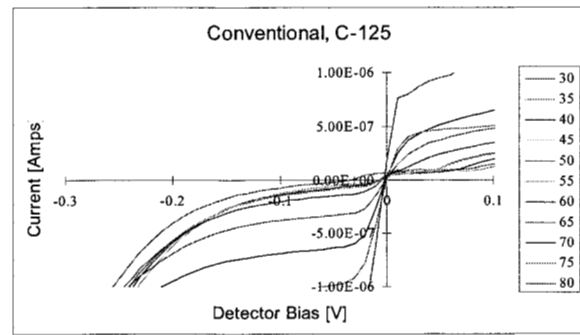
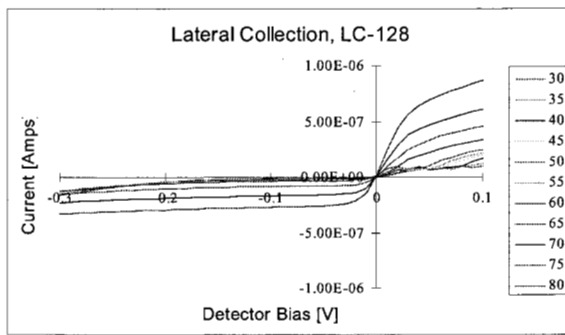


Figure 7.0. - Comparison of IV curves for DLPH lateral collection and conventional designs from 30 K to 80 K

The TES lateral collection diode layout is illustrated in abbreviated form in Fig. 8.0. The design consists of a hexagonal array of $7\mu\text{m}$ diameter implanted circles on $20\mu\text{m}$ center-to-center spacing. The total electrical junction area is $5.7 \times 10^{-5} \text{ cm}^2$, a $\sim 10\text{X}$ reduction compared to the pixel

area. Using the theoretical analysis of Holloway⁶, for hexagonally configured lateral collection diodes, the internal quantum efficiency of this layout is calculated to be 93% for a $16\mu\text{m}$ diffusion length and 97% for a $25\mu\text{m}$ diffusion length.

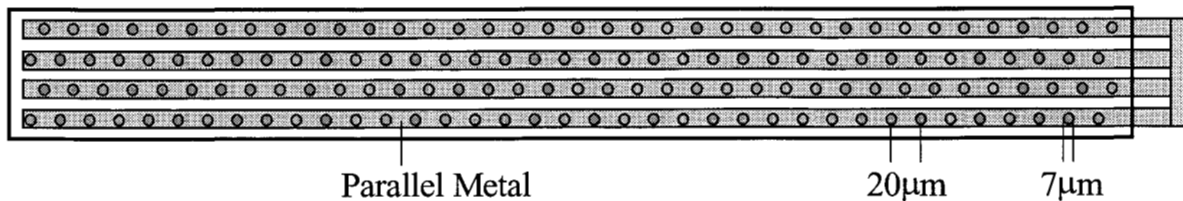
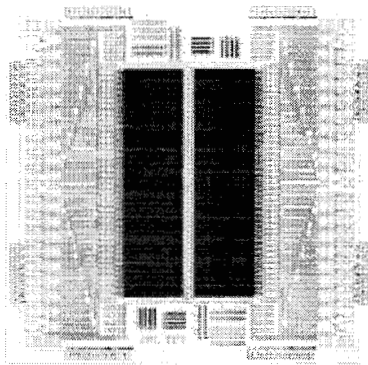


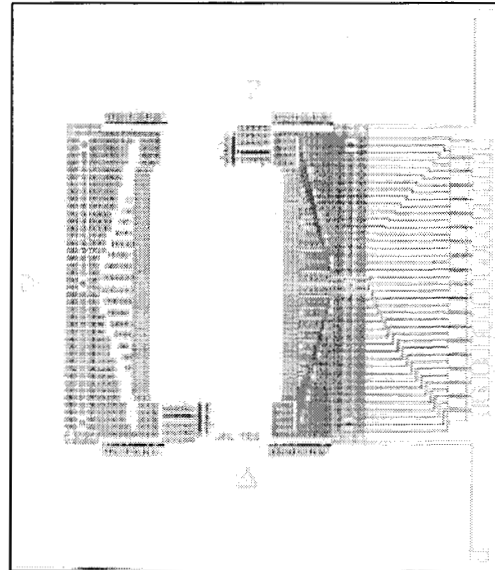
Figure 8.0 - Layout of a lateral collection pixel an array of $7\mu\text{m}$ diameter diodes on $20\mu\text{m}$ centers.

The detector arrays for the TES program are linear arrays consisting of sixteen $75 \times 750 \mu\text{m}^2$ diodes on $75 \mu\text{m}$ pitch. The chip layout design is illustrated in Fig.9.0 (a). For redundancy two 1×40 arrays are included on each chip, which measures $4.25 \times 4.45 \text{ mm}^2$. All 80 diodes are brought out to probe pads for on-wafer cryoprobng.

The cryoprobe pads are placed near one edge of the wafer, allowing 100% on-wafer testing. The best 1×16 detector array is determined from the 77K cryoprobe data. The selected detector die is hybridized to a sapphire fanout chip for mounting onto the CMLB. The $6.7 \times 7.8 \text{ mm}^2$ fan-out layout is shown in Fig. 9.0 (b).



(a)



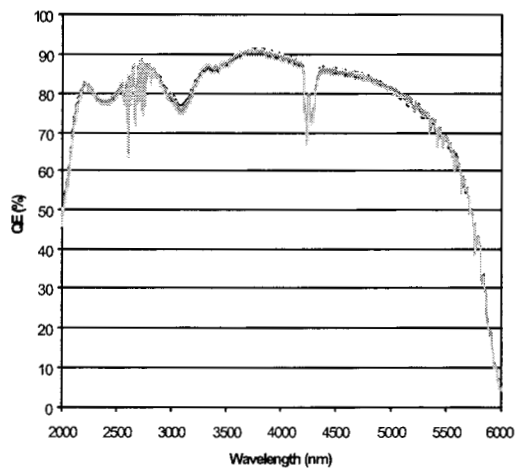
(b)

Figure 9.0 - (a) Layout of detector chip with of two, 1x40, detector columns and cryoprobe pads. (b) Sapphire fanout

5.0 DETECTOR ARRAY PERFORMANCE

The performance of the photodiodes is measured by the current-voltage and signal response behavior. RoA are derived from these IV curves and presented here. External quantum efficiency and relative spectral response are combined to provide spectral quantum efficiency. All the data was collected at 65 K.

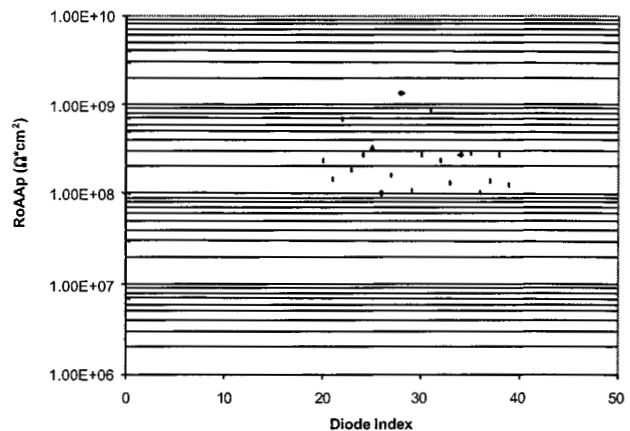
Band 1A - The electrical and optical performance of 20 consecutive Band 1A detectors in an array qualified for integration into the IRFPA is shown in Fig. 10.0. The median R_0A is $1.9E8 \text{ ohm-cm}^2$. The median QE, measured at $3.5 \mu\text{m}$, is 87.5%. The cut-off wavelength is $5.81 \mu\text{m}$.



The pixel to pixel uniformity for these large area detectors is excellent. The structure (slowly varying) observed in the spectral response data for λ less than $3.5 \mu\text{m}$ is due to the interference effects of the broadband AR coating. Also apparent in the data are atmospheric absorption bands due to CO_2 and H_2O .

Band 2A - The electrical and optical performance of 21 consecutive Band 2A detectors in an array qualified for integration into the IRFPA assembly is shown in Fig. 11.0. The median R_0A is $1.4E4 \text{ ohm-cm}^2$. The median QE, measured at $9.02 \mu\text{m}$, is 70.2 %. The cut-off wavelength is $10.4 \mu\text{m}$.

Figure 10.0 - R_0A and spectral QE measurements for a Band 1A detector array.



As in the Band 1A, the pixel to pixel uniformity for these large area detectors is excellent with the measured R_0A being very close to the theoretical limit. Apparent in the data are several atmospheric water, absorption bands.

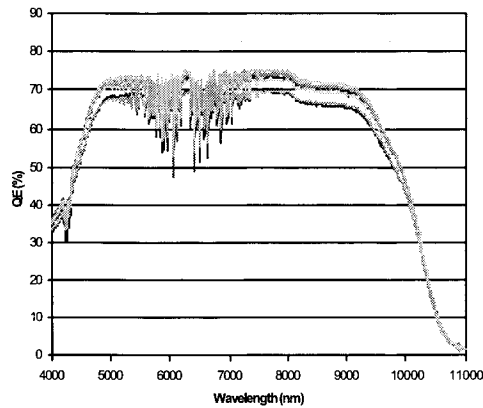


Figure 11.0. - R_0A and spectral QE measurements for a Band 2A detector array.

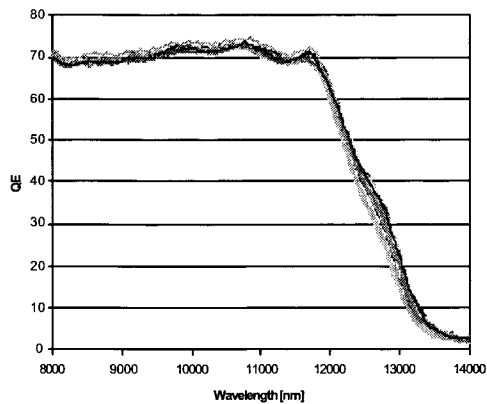
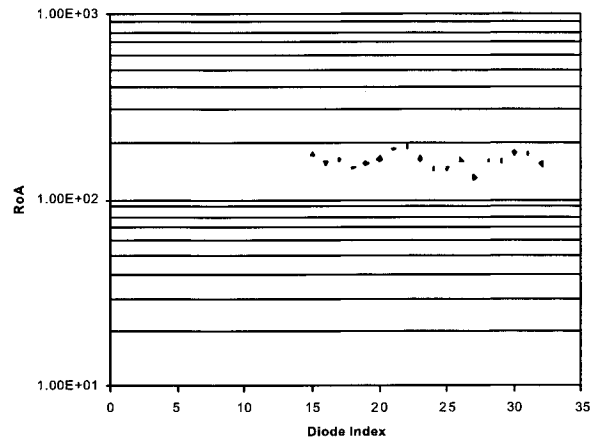
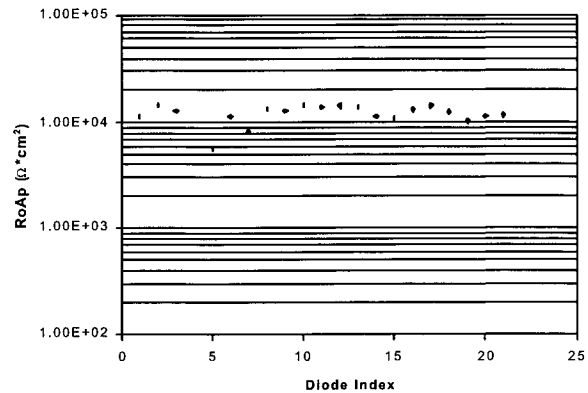


Figure 12.0. - R_0A and spectral QE measurements for a Band 1B detector array.

The pixel to pixel uniformity for these large area detectors is also very good with the measured R_0A being a factor of two below theory. Note the lack of atmospheric absorption features in this well-known atmospheric window.

Band 2B - The electrical and optical performance of 18 consecutive Band 2B detectors in an array qualified for integration into the IRFPA assembly array is shown in Fig. 13.0. The median R_0A is 5.2 ohm-cm². The median QE, measured at 14.0 μm , is 57 %. The cut-off wavelength is 15.75 μm .

Band 1B - The electrical and optical performance of 18 consecutive Band 1B detectors in an array qualified for integration into the IRFPA assembly is shown in Fig. 12.0. The median R_0A is 1.4E2 ohm-cm². The median QE, measured at 9.02 μm , is 63.4 %. The cut-off wavelength is 12.9 μm .



The pixel to pixel uniformity for these large area detectors is also very good with the measured R_0A being a factor of two to three below theory.

Figure 14.0 summarizes R_0A data from all hybrids fabricated for all four TES bands. Median R_0A is plotted as a function of the measured cut-off wavelength. Each open circle data point represents the measured median value for a different hybridized array. The dashed line is the theoretical R_0A calculated using a 1-dim model and using measured materials parameters.² The solid triangles are the detector performance flowed down from IRFPA performance requirements. The data shows performance very close to the diffusion limited theoretical performance except for the shortest wavelength band.

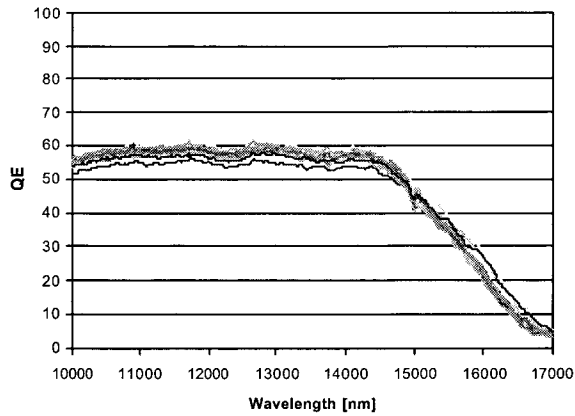


Figure 13.0. - R_0A and spectral QE measurements for a Band 2B detector array.

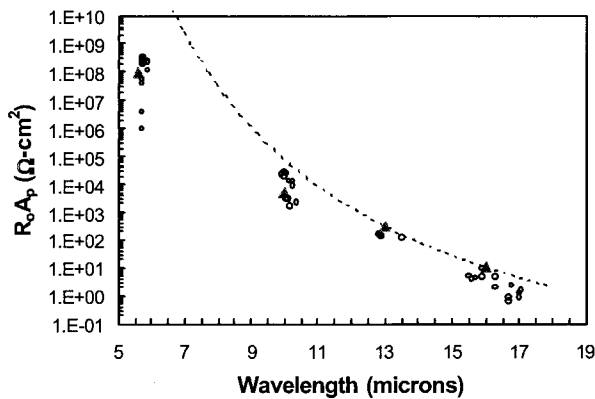
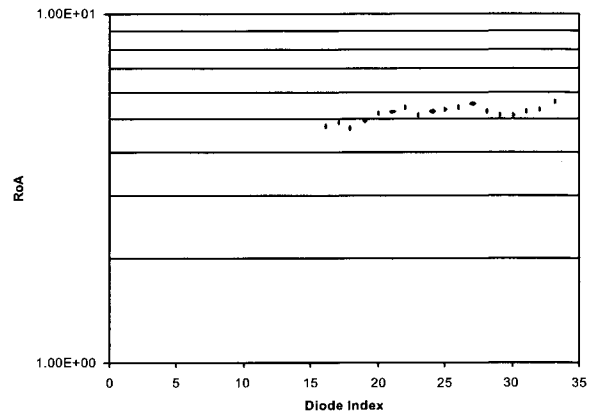


Figure 14.0. - R_0A_p Vs Cutoff

In order to reduce the effect of J-FET voltage noise upon the detectivity of the IRFPA in the 2B band, these detectors are operated with a small reverse bias. Operating in reverse bias significantly increases the detector impedance and reduces this noise contribution. Noise spectral densities are shown in figure 15.0 for a number of 2B detectors for 15mV of reverse bias. At this voltage bias about 1.0 microampere of current is generated. The resultant alpha term from Tobin⁷, is quite small ($\sim 2.0E-5$ for $n=1$) although significant $1/f$ noise is observable. The lowest electrical frequency of interest in the 2B band is 2.0 kHz. Noise power at frequencies lower than this is electrically filtered and will not add appreciably to the rms noise when sampled at the A/D converter.

Two-dimensional spatial response measurements were taken on sample arrays of each band. The measurements were made at 65K with a 1.35-micron YLF laser focused to a small spot with less than 7-micron extent. Adjacent

detectors were grounded and the signal from the detector recorded as the laser was stepped across the pixel.

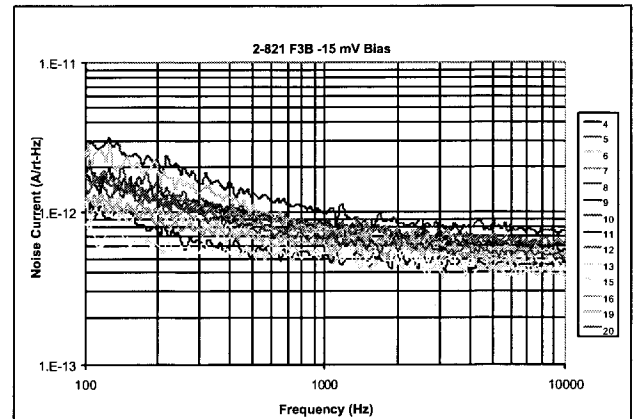


Figure 15.0. - Noise spectral density Band 2B detectors

Clearly visible in the surface plots for this 1A-band pixel (Figure 16.0) is the extended tail of response out side of the desired optical area⁸. An implanted region was designed to border the pixel, but apparently, for reasons not completely understood, this guard band is not functioning efficiently. The effect is significantly lesser for the longer wavelength devices to the extent that it is not visible in the 1B or 2B bands. This apparent dependence on band gap is not understood. Although, it has been suggested that this effect may be due to the increased spreading resistance of the As implanted guard-band in higher band-gap, lower conductivity, HgCdTe film.

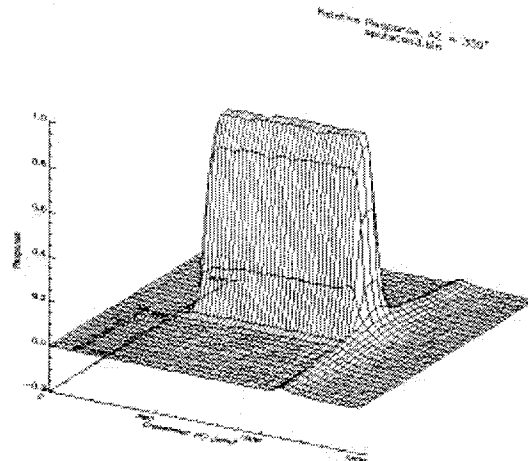
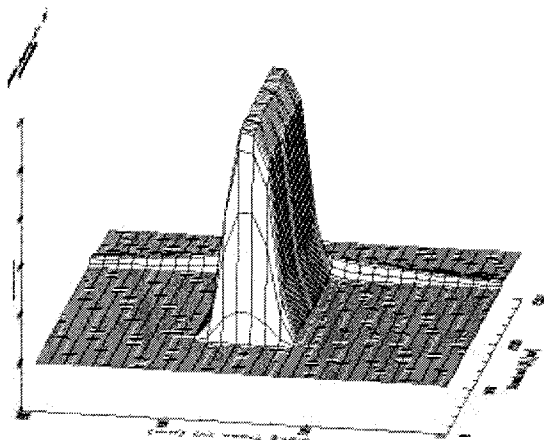


Figure 16.0. - 2-D response maps for a 1-A band pixel.

6.0 PREAMPLIFIER DESIGN

Figure 17.0 shows the basic topology for the transimpedance amplifier used in the IRFPA. In that this design is a current amplifier it is easiest to consider the noise of the amplifier in terms of its current noise components referred to the summing node.

For the 1B IRFPA the source follower loads, R_s , will be mismatched to provide the required offset in the J-FET differential pair (U401). A bleed resistor (not shown) is supplied to remove the voltage offset at the output due to the detector reverse bias current. The dominant noise current terms at the summing node are given by equation 1.0. In this equation we have the usual terms for signal photon shot noise, detector dark current shot noise, detector dark current 1/f noise and the thermal noise of both the detector and the feedback resistor. In addition, the voltage noise of the J-FET is included as two current terms resulting from an interaction with the detector resistance and capacitance.

$$i_n(f) = \sqrt{\frac{4kT_d}{R_f} + \frac{4kT_d}{R_d} + \left(\frac{e_n(f)}{R_d}\right)^2 + \left[(f/2\pi) \cdot e_n(f) \cdot C_T\right]^2 + \frac{4kT_d}{f} + 2qI_d + 2qI_{ph}}$$

Equation 1.0

It should be noted that the detector capacitance term here, C_T , includes all sources of capacitance at the summing node. It is also assumed that the source follower gain is near unity.

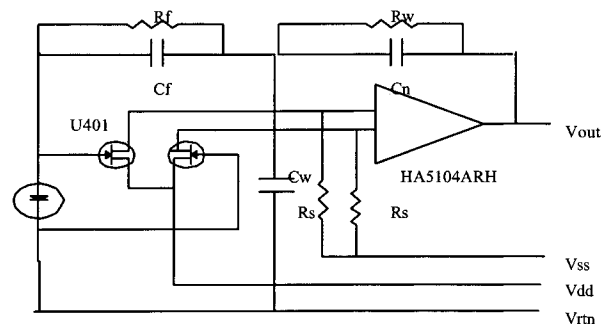


Figure 17.0 IRFPA schematic

7.0 RADIATION TESTING

The total integrated dose (TID) levels for the TES orbit (98°, 705km) have been determined to be equal to 10Krad (Si) with 100 mils, equivalent, aluminum shielding over five years. A transport analysis has been performed using an instrument mass model taking into account the effect of instrument materials and geometry upon the TID level. For the IRFPA the TID was determined to be 3.5Krad (Si), worst case. Applying the radiation design margin (x2) results in a requirement of 7.0 Krad (Si) for the IRFPA.

Testing was performed at the Maxwell, Co-60, Range Source in San Diego, CA for one IRFPA assembly. Maxwell performed the Pulse Height Distribution (PHD) testing and the dosimetry. Maxwell assisted Rockwell in integration of the IRFPA Assembly and test electronics with the irradiation facility to provide for TID testing and PHD testing. Rockwell

performed the functional testing after dose increments. The objective was to study gamma total ionizing dose (TID) and pulse height distribution (PHD) effects in a TES IRFPA Assembly, consisting of detector array, J-FETs, feedback resistors, and feedback capacitors. Rockwell provided the IRFPA Assembly in a cryogenic Dewar.

The warm electronics were located outside the dewar behind lead shielding. One IRFPA was tested. Temperature was maintained at ~ 80 K during the irradiation and testing. Testing consisted first of low flux gamma irradiation to measure pulse effects, followed by standard dose rate Co-60 gamma irradiation for total ionizing dose. Figure 18.0 shows the IRFPA response and offset as a function of total dose for eight channels.

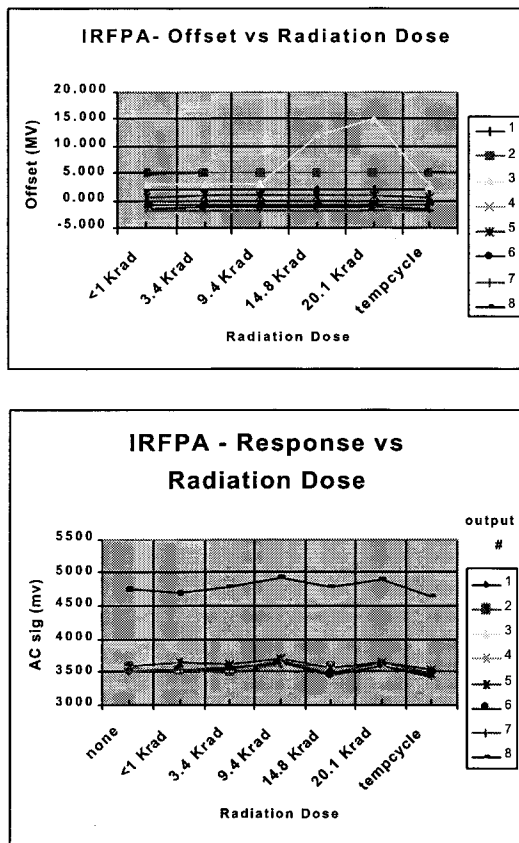


Figure 18.0 - IRFPA response and offset as a function of total dose.

For PHD testing the dose rate was adjusted to 0.03 Rad (Si)/s by locating the dewar to position the FPA at 120 inches from the source. The estimated gamma flux was $6E7$ ph/cm²-s. Data collection runs were typically for 300 s, resulting in a run fluence of $1.8E10$ ph/cm². Figure 19.0 shows plots of

pulse height versus channel for three detectors with channel calibration data.

Of the 8 pixels tested only one showed anomalous behavior. Pixel three had been identified as a “bad pixel” due to its much lower RoA. It has been suggested that a local passivation defect may be the cause of the low RoA and the increase in noise and offset for that pixel beginning at <9.4 Krads TID. Pixel number eight’s neighbor was left ungrounded for this test and as a result its effective optical area is much larger than the other pixels resulting in increased photo-response. This is consistent with lateral collection mechanism described earlier. Further efforts will be made to interpret the PHD data for the EOS orbit with corrections for gamma Vs proton LETs.

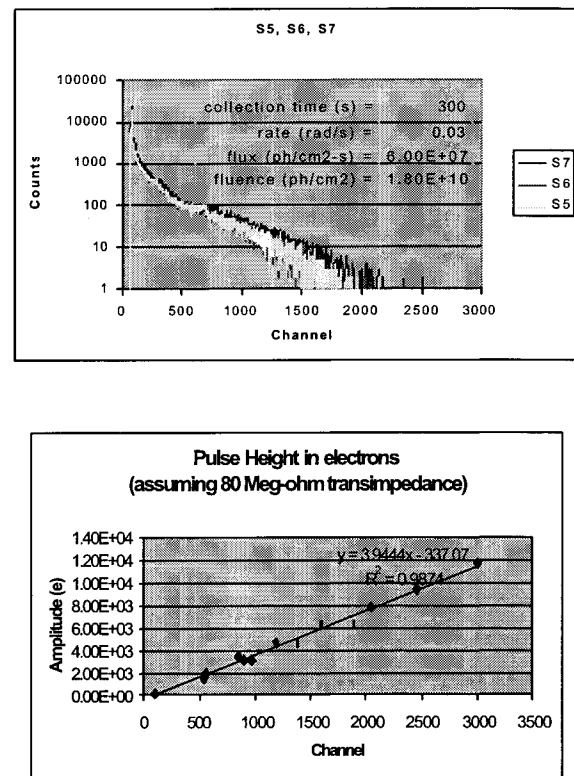


Figure 19.0 - Pulse height versus channel for three detectors and channel calibration data.

6.0 SUMMARY

The TES program specifications of 65K operating temperature and $75 \times 75 \mu\text{m}^2$ pixel size place rigorous requirements on material quality. Improvements in the materials growth, coupled with the lateral collection diode approach, have produced significant performance improvements for these detectors over a broad spectral

range. This performance has been demonstrated on multiple die for each band. Qualified detector arrays for each band are currently being integrated with the electronics. Further reductions in junction area may be possible with the use of micro-lens technology. Using this technology the above detector might realize an additional 4x reduction in junction area and capacitance. For this to occur the spatial response of the micro-lens needs to be better understood. Also the performance of the micro-lens in very narrow band illumination needs to be characterized to ensure that etalon or "channeling" effects are not present.

ACKNOWLEDGEMENT

The work described in this article was performed both at the Jet Propulsion Laboratory, California Institute of Technology and at its subcontractors under contract with the National Aeronautics and Space Administration.

Reference herein to any specific commercial product, process, or service by trade name, trade mark, manufacturer, or otherwise, does not constitute or imply its endorsement by the United States Government or the Jet Propulsion Laboratory, California Institute of Technology.

REFERENCES

- 1 Reinhard Beer, TES, Scientific Objectives & Approach, Goals & Requirements Rev. 6, (1999)
- 2 J. Bajaj, et al, IRIS Specialty Group Infrared Detectors, ERIM, (1999).
- 3 W.V. McLevige, et al, 1996 IRIS Specialty Group Infrared Detectors, ERIM, (1996).
- 4 R. J. Briggs, Three-Dimensional Numerical Analysis of Diffusion Current and Quantum Efficiency of Small Area $\text{Hg}_{1-x}\text{Cd}_x\text{Te}$ Photodiodes, IEEE, (1981)
- 5 Jet Propulsion Laboratory, National Aeronautics and Space Administration, Contract 960577, (1996)
- 6 H. Holloway, *J. Appl. Phys.*, **49**, 4264, (1978)
- 7 S.P. Tobin, *IEEE Transaction*, ED-27, p. 43, (1980)
- 8 Internal Communication, Jet Propulsion Laboratory, David Rider, (1999)